Probabilistic Ultrasound C-scan Imaging of Barely Visible Impact Damage in CFRP laminates

Jeroen Vandendriessche[1], Adil Han Orta[2], Erik Verboven[1], Wim Van Paepegem[1], Koen Van Den Abeele[2] and Mathias Kersemans[1,#]

[1] Mechanics of Materials and Structures (UGent-MMS), Department of Materials, Textiles and Chemical Engineering (MaTCh*)*, Ghent University, Technologiepark-Zwijnaarde 46, 9052 Zwijnaarde, Belgium

[2] Wave Propagation and Signal Processing (WPSP), Department of Physics, KU Leuven – Campus Kulak, 8500 Kortrijk, Belgium

[#] Corresponding author: Mathias.Kersemans@UGent.be

Abstract

Ultrasonic pulse-echo C-scan imaging is a widespread method for detecting and characterizing defects in fiber reinforced polymer composites. However, the accurate assessment of a complex distributed damage cluster, like barely visible impact damage, in multi-layer and heterogeneous composites is not straightforward. For reliably estimating the remaining load carrying capacity and/or remaining useful lifetime of a damaged composite, a proper and complete damage assessment is of utmost importance. In this paper, a statistical time-energy gating approach is proposed in view of obtaining improved ultrasonic pulse-echo imaging of impacted composites. The majority of virgin A-scan signals are first clustered by analyzing their back-wall echoes. Next, using the principle of maximum likelihood, a Rice distribution is matched to the instantaneous amplitude in order to estimate the natural variability in the local energy of the virgin response signals. The resulting time-varying reliability interval provides an effective means to identify signals coming from defects or inhomogeneities, and as such to robustly assess defect parameters. The proposed probabilistic imaging procedure is demonstrated on various carbon fiber reinforced polymer laminates with barely visible impact damage. The obtained results are benchmarked by conventional ultrasonic C-scan imaging in through-transmission mode as well as in pulse-echo mode using the classical time gating approach. In contrast to the classical time gate method, the proposed statistical time-energy gating procedure successfully extracts and quantifies the full extent of the complex impact damage cluster. Further, the good noise resistance of the proposed probabilistic imaging method is demonstrated for a wide range of signal-to-noise ratios.

Keywords

CFRP, BVID, Pulse-echo, Ultrasound, Rice distribution, Maximum Likelihood Estimation, statistical time-energy gate

1. Introduction

Carbon Fiber reinforced polymer (CFRP) laminates, or composites, are increasingly being used in industry thanks to their high specific strength and stiffness, good corrosion resistance and tailorability. However, as a result of their layered structure, these materials are susceptible to internal damage phenomena which may be introduced during both the manufacturing stage and in-service lifetime. To

assure the structural integrity of a composite part, it is crucial to apply appropriate non-destructive testing (NDT) techniques. Several NDT techniques have been developed over the years, making use of various physical principles: vibrational testing [1, 2], (vibro-)thermography [3, 4], shearography [5, 6], guided elastic waves [7-9] and ultrasonics [10-12], amongst others.

The ultrasonic pulse-echo technique is perhaps the most widespread NDT technique for the inspection of composites, and has been successfully applied for the estimation of local fiber orientation and content [13], and for the localization of porosities [14], inserts [15] and delamination damage [10]. For complex damage features in composite laminates, accurate imaging is a challenging task due to interlaminar scattering, high damping losses, wave dispersion, material heterogeneity and structural noise [16]. An example of such a complex damage is barely visible impact damage (BVID). This type of damage is typically caused by a low-velocity impact which induces a cluster of cracks and delaminations throughout the depth of the composite [17]. Typically, such BVID extends as a damage cone through the depth, resembling a double helical pattern [10, 17]. For the development and subsequent validation of advanced FE damage models simulating composites subject to impact loads [18], it is crucial to have experimental tools for proper imaging and assessing BVID. Also, for understanding the evolution of impact damage under various load regimes [19-22], and the correct prediction of the residual lifetime of the impacted composite, good knowledge on the BVID phenomenon is required. The complexity of BVID for inspection methodologies is that it contains both shallow and deep defects (of which the projected areas partially overlap). In pulse-echo ultrasound, the shallow defects often remain undetected due to the dominance of the high-amplitude front wall echo (FWE) [23, 24]. The echo of deep defects on the other hand may undergo significant pulse distortion and broadening, and is often obscured by the back wall echo (BWE) and/or structural noise [16, 25]. Due to the physical size of the ultrasonic beam, diffraction effects and structural noise, small defect fragments close to each other, or neighboring delaminations at different interfaces, may be difficult to spatially resolve [26]. Several techniques exist to mitigate these challenges.

In spatial domain, techniques to improve the quality of the ultrasonic dataset include averaging procedures, spatial deconvolution approaches and median filtering. A straightforward approach is the use of high ultrasonic frequencies, e.g., 50 MHz, in order to increase both the spatial and depth resolution [10]. Though, this comes with the obvious drawback that the inspection depth becomes limited due to excessive attenuation of the high-frequency waves in the multi-layer composite. A possible solution to the limited depth range could be the use of double-sided inspection [27], but this is on the expense of a more involved experimental procedure. In [28] and [29], the point-spread function of ultrasonic pulse-echo imaging is computed and used in different deconvolution schemes to enhance spatial resolution. In [30], an axially varying kernel forward convolution model is applied for the deconvolution of ultrasonic imaging yielding enhanced results over fixed-kernel methods. In [26], various morphological techniques to reconstruct the size of impact damage in composites are compared. Although these techniques can enhance the imaging quality, they rely on several simplified assumptions and/or experience difficulty when applied on multi-layer composites.

Different approaches in time and/or frequency domain have been proposed to suppress noise features, including cross-correlation, frequency filtering and deconvolution schemes [23, 31, 32]. In [12, 33, 34], autoregressive spectral extrapolation was considered to enhance the signal-to-noise ratio (SNR) and time-resolution of pulse-echo signals. The developed methods show good performance, but have still difficulty to assess deep plies in composite laminates due to attenuation and pulse distortion.

The effects of wave attenuation can be partially addressed by the use of a distance-amplitude correction (DAC) function, which is typically established by the use of multiple calibration measurements [35, 36]. Especially for homogeneous materials with low structural noise, such as classical metals, this approach works well. For heterogeneous media however, such a DAC function magnifies structural noise features. Further, it cannot cope with frequency-dependent attenuation which leads to dispersed wave signals. Other researchers have employed multiple time gates at different depths in order to obtain a collection of through-depth damage maps by analyzing pulse-echo and backscattered signals [37, 38]. It provides rich information, but the interpretation becomes more involved if the internal plies in the composite are not perfectly straight. A proper selection of the time gate settings, such as width and position, is crucial. Space dependent thresholds, coupled to synthetic aperture focusing technique, have been proposed for improved assessment of damage [39]. The method was demonstrated for the detection of submillimeter defects in strongly scattering metallic media. Though, the authors indicate also few limitations of their developed technique: (i) difficulty to detect deep defects having a weak defect echo, (ii) overestimation of defect size and (iii) false defect indications due to the presence of creeping waves. The detection of flaws in stainless steel specimens exhibiting high grain noise, due to microstructure, has been done by considering extreme value statistics [40, 41].

Further, researchers applied advanced classification and processing schemes directly to the full 3D ultrasonic dataset to create superior quality images, offering improved detectability and depth estimation of defects. A machine learning approach was applied to ultrasonic pulse-echo data in order to identify the level of carburization in industrial steel pipes [42]. Neural network-based classification of pulse-echo signals from composite materials was proposed in [15]. Likewise, improved detection and depth estimation of delamination inserts in CFRP was reported using wavelet decomposition and deep convolutional neural networks [43]. Though, one of the associated difficulties to deep learning approaches is its generalization to datasets obtained under different conditions, e.g., changed experimental settings, different material and/or defect type. Recently, a planar Ultrasound Computed Tomography method [44] has been proposed for interpreting 3D ultrasonic data. This novel method relies on advanced tomographic reconstruction methods, and was demonstrated on a 24-ply CFRP laminate with BVID. It was shown that it not only extracts information on the BVID, but also provides a full 3D reconstruction of the fiber architecture of the composite laminate.

Although many contributions have been proposed in literature to improve ultrasonic damage imaging in a range of materials, the accurate inspection and characterization of a complex damage cluster, such as BVID, in composites remains a challenge. This is attributed to the heterogeneous and multi-layer structure as well as the visco-elastic behavior of typical composites. Also, the typical through-depth damage distribution in case of BVID adds significant complexity.

In this paper, a probabilistic method for improved imaging and quantification of complex damage features in multi-layer composites is introduced. Instead of applying a classical time gate on the ultrasonic pulse echo data, the proposed method employs a statistical time-energy gating (STEG) approach. The instantaneous amplitude of the recorded ultrasonic signals is fitted by Rice distributions in order to capture the natural variability of the composite laminate. The resulting time-dependent reliability intervals are used to differentiate between healthy and defect signals.

The paper is structured as follows. In section 2, the investigated samples and experimental procedure are discussed. Section 3 provides the outline and the details of the proposed statistical time-energy

gating STEG method. Section 4 discusses the performance and the robustness of the novel STEG algorithm for various inspection conditions. Finally, conclusions are formulated in section 5.

2. Materials and method

The studied CFRP laminates have an approximate thickness of 5.5 mm and consist of 24 unidirectional plies which are stacked according to different stacking sequences. The material is a combination of polyacrylonitrile based carbon fibers with PYROFIL #360 resin having a density of 1200 kg/m^3 and a glass transition temperature of 170 °C. This resin is modified to allow curing in under 5 min, with a gel time of 200 s at 130 °C. The laminates are manufactured using compression molding for 7 minutes at 140 °C and a pressure of 8 MPa, resulting in a fiber volume fraction of close to 60%. The manufactured specimens are cut to size 150x100 mm^2 using a waterjet and are conditioned to reduce the effect of moisture on the results. The three CFRP samples have then been impacted by a 7.72 kg drop weight at different heights according to ASTM standard D7136 [45]. This resulted in the formation of barely visible impact damage BVID. Table 1 shows the specifications of the different samples, as well as the measured impact energies.

Table 1: Tested samples

Name	Thickness	Stacking sequence	Impact height	Impact energy
CFRP-1	5.5 mm	$[+45/0/-45/90]_{3s}$	0.1 m	5.4 J
CFRP-2	5.5 mm	$[0/90]_{6s}$	0.1 m	6.0 J
CFRP-3	5.5 mm	$[+45/0/-45/90]_{3s}$	0.3 m	15.5 J

A focused immersion transducer (type GE H5M) of diameter 5 mm with nominal center frequency of 5 MHz and focal distance of 25.4 mm is employed. A reference measurement of the transducer's impulse response in both time and frequency domain is shown in Figure 1.

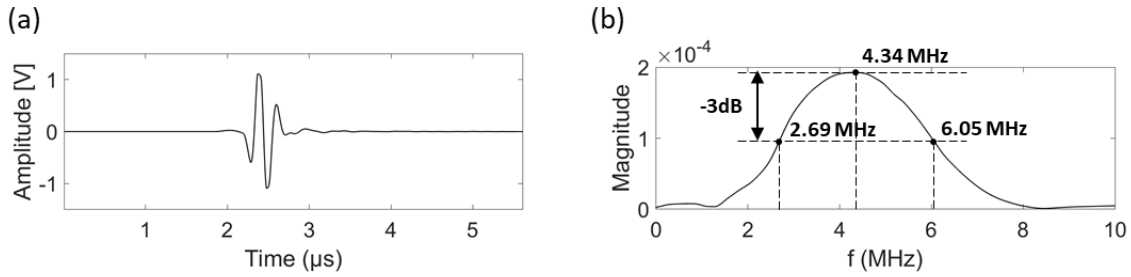

Figure 1: Impulse response of employed GE H5K transducer in (a) time and (b) frequency domain

The samples were inspected using an in-house developed immersion pulse-echo ultrasonic test setup, a schematic layout of which is shown in Figure 2.

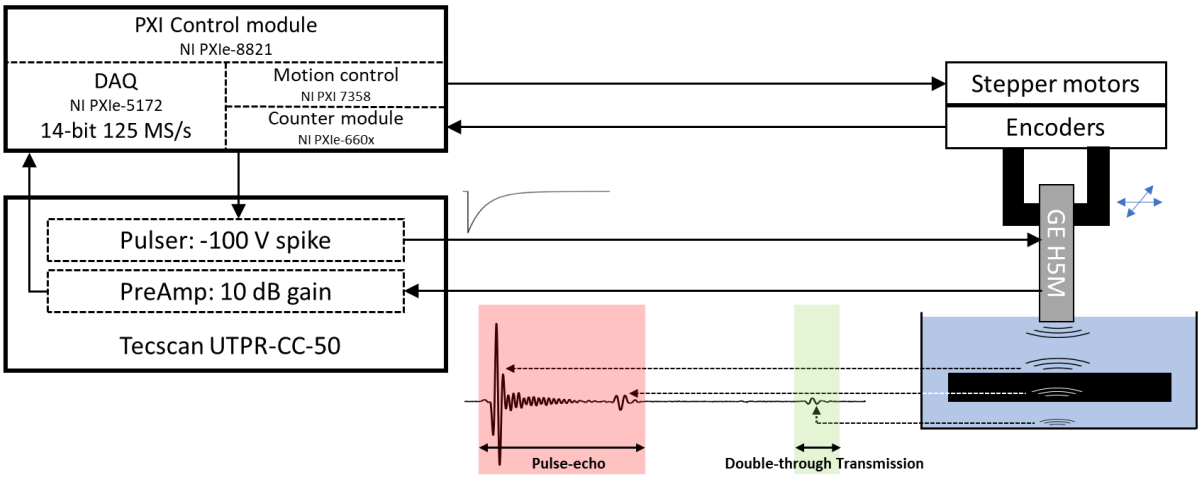

Figure 2: Schematic layout of experimental procedure

The transducer is mounted on a 3-axis scanner at a distance of 18 mm from the front surface (focus point in middle of sample). It was moved along an XY-grid with increments of 0.2 mm at a speed of 20 mm/s using motion control (NI PXI 7358) and counter module (NI PXIe-660x) cards embedded in a PXI Express Chassis (NI PXIe-1078). A TecScan UTPR-CC-50 pulser was used to excite the transducer (pulse settings: 100 V negative spike excitation, 45 Ohm internal resistance and 1070 pF damping capacity). Response signals were pre-amplified by 10 dB and sent to a 14-bit oscilloscope (NI PXIe-5172) for sampling at 125 MS/s. The recorded response signals have a SNR of ~32 dB. The system is controlled by an embedded controller (NI PXIe-8821) with an interface programmed in LabView 2018. After the scan has finished, the recorded 3D (x,y,t) ultrasonic dataset is processed in Matlab R2020b. Both the pulse-echo and the double through-transmission signals, i.e., the reflection from the bottom of the water tank, are acquired by considering a sufficiently long recording time (see red and green area in Figure 2).

The amplitude C-scan representation of the double through-transmission signal of sample CFRP-1 is shown in Figure 3. This C-scan clearly outlines the extent of the induced impact damage, however, it does not provide any depth-information on the complex BVID cluster. As readily known from literature, the through-transmission technique is considered to be an accurate method to determine the overall size of impact damages [46]. Defect sizing based on ultrasonic C-scans is usually done by using an amplitude drop method. Different thresholds can be used, of which the 6 dB amplitude drop (or equivalent 3 dB intensity drop) is used most often. This threshold value was originally proposed and commonly accepted for pulse-echo imaging, for which a 6 dB amplitude drop is expected to coincide with the edge of the defect [47, 48], even though several reports have shown that the 6 dB amplitude drop method risks undersizing the defects [49-51]. Therefore, the damage area in this paper has been extracted from the double through-transmission C-scan signals using a conservative 3 dB amplitude drop threshold. The resulting damage area has been added to Figure 3 with a dashed black line. Of course, there will always be some uncertainty in the exact dimensions of the defect due to the nature of ultrasonic inspection (finite beam width, diffraction, noise) [16]. In the remainder of the paper, this extracted damage contour from the double through-transmission signal will be considered the ground-truth, and will be superposed on further generated C-scan images for comparative analysis. The four

numbered spots (1 to 4) indicated on the Figure 3 will be used to explain the obtained results in the next section.

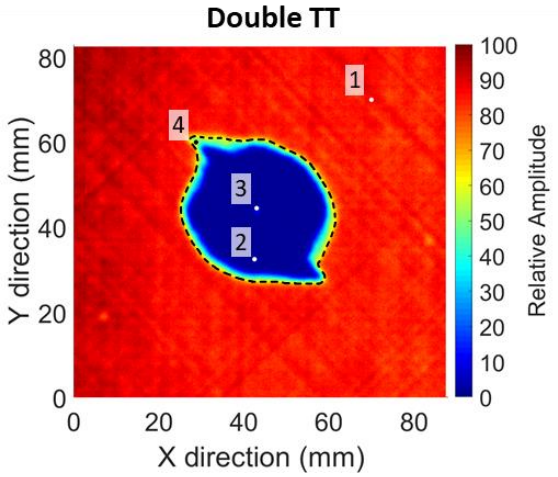

Figure 3: Amplitude C-scan image in double through-transmission mode for sample CFRP-1. The damage contour (3 dB amplitude drop) is superposed as a dashed black line.

3. Pulse-echo mode

3.1. Classical time gate (TG)

In Figure 4.1, a typical A-scan signal for a non-damaged (virgin) scan point (see indicator 1 on Figure 3) is shown. After the strong front wall echo FWE, the heterogeneous and layered structure of the composite laminate produces small echoes which become gradually weaker with depth. About 4.5 µs after the FWE, the back wall echo (BWE) is observed which is 180° phase reversed and shows some signal distortion due to frequency dependent attenuation. The A-scans for the other 3 scan points, which are located within the damage area (see indicators 2-4 in Figure 3), are displayed in Figures 4.2-4.4.

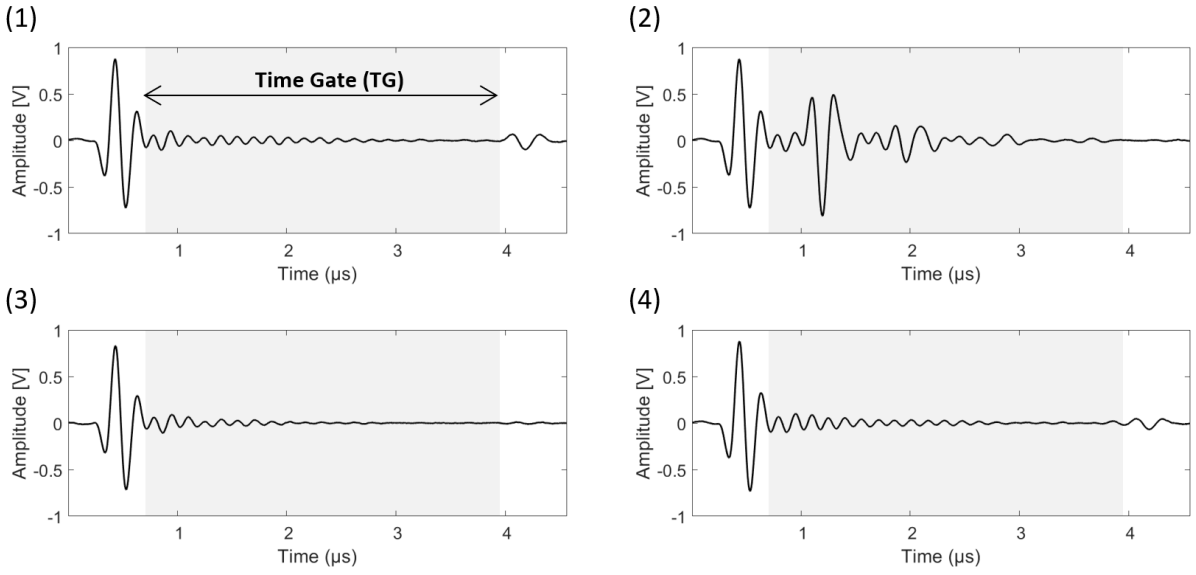

Figure 4: A-scan signals at different locations on the sample CFRP-1 (see indicators 1-4 in Figure 3). The grey area indicates the used time gate for C-scan imaging.

A classical time gate (TG) was superposed on the pulse-echo A-scan signals (grey area in Figure 4). A correct choice of this time gate is not straightforward [52]: (i) if the TG is put too much to the left, it gets dominated by the tail of the FWE, (ii) if the TG is put too much to the right, it gets dominated by the onset of the BWE, and (iii) if the TG is taken too short, information is missing from certain depths. The shown TG in Figure 4 has been selected by trial and error in order to balance between these three factors. With this TG on the pulse-echo A-scan signals, the amplitude and Time-of-Flight (TOF) C-scan representations can be obtained. After cross-correlating the response signals with the reference pulse (Figure 1a), the amplitude C-scan is constructed by evaluating the maximum instantaneous amplitude within the time gate. The TOF C-scan is found by evaluating the time instance associated with this maximum instantaneous amplitude. For the remainder of the manuscript, the TOF C-scans are converted to depth C-scans by employing the longitudinal ultrasonic velocity in the depth direction of the composite. The resulting amplitude and depth C-scans are represented in Figure 5.

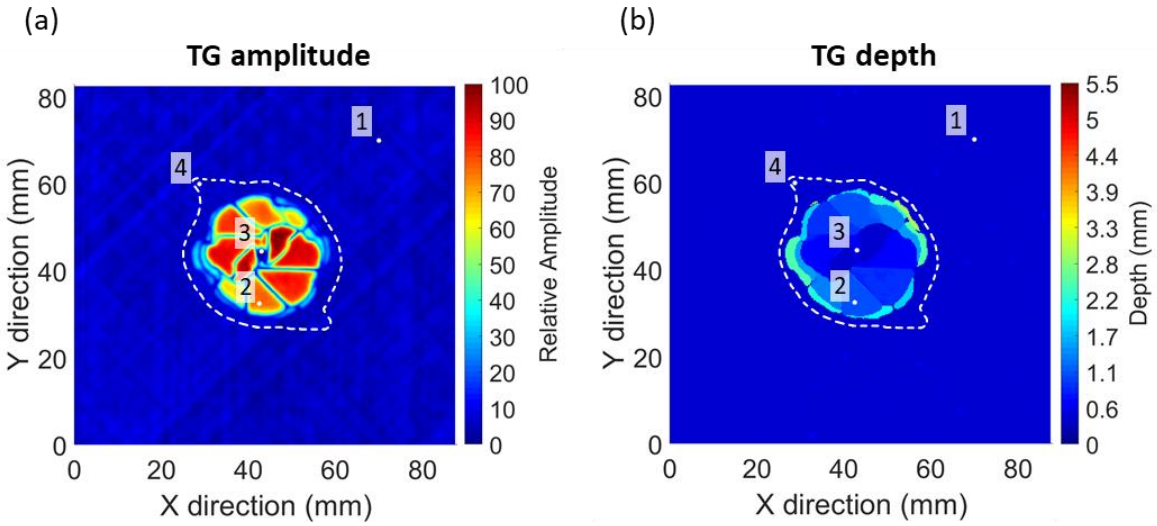

Figure 5: (a) Amplitude and (b) depth C-scan image for sample CFRP-1 using a classical time gate TG. The damage contour, extracted from the double-through transmission amplitude C-scan, is superposed as a white dashed line.

In the virgin area, effects of the stochastic heterogeneity and the multi-layered structure of the investigated CFRP can be noticed by the variations in the background, especially for the amplitude C-scan image (Figure 5a). At the impact zone, these pulse-echo C-scan images allow to estimate the 3D structure of the impact damage. However, comparison with the extracted damage contour of the double through-transmission result (see the superposed dashed white line in Figure 5) reveals that these pulse-echo C-scan images fail to show the full extent of the barely visible impact damage. Part of the BVID is simply not represented in these pulse-echo C-scans, in particular:

(i) The innermost area of the impact damage (at location of impact event) which is expected to consist of very shallow delaminations.

(ii) The outermost area of the impact damage which is expected to consist of very deep delaminations.

(iii) The neighboring delamination fragments do not always connect each other, and appear to have gaps in-between.

To understand the underrepresentation of these features, a few characteristic A-scan pulse-echo signals (see Figure 3, points 2 to 4) at different locations in the damage area were assessed in more detail. The A-scan signal at point 2 (see Figure 4.2) shows a clear defect echo between the FWE and BWE from which the amplitude and associated depth can be easily extracted. Things change when evaluating the A-scan signal at point 3 (see Figure 4.3), which is close to the location where the impact weight hit the CFRP sample. There is no clear defect echo to be observed. The reason for this is that only very shallow delaminations are expected at the location of impact. Hence, the defect echo (partially) coincides with the dominant FWE. Although this commonly leads to a slight deviation of the signal in shape or amplitude, it clearly cannot be captured using a classical time gate approach. Therefore, the pulse echo C-scan images obtained with a classical time gate yield no indication of a defect at that location. Finally, also the pulse-echo signal at point 4 is of particular interest (see Figure 4.4). This point 4 is located close to the outer edge of the impact damage, and as such it is expected to correspond to very deep damage. Plain visual analysis of the A-scan signal reveals no noticeable changes compared to the A-scan signal of virgin scan point 1. The reason for this is that echoes originating at very deep features are quite low in amplitude and are therefore naturally obscured by the structural noise in the signal, and/or (partially) coincide with the BWE. As such, the classical time gating procedure has difficulty in capturing these deep damage features. To underline this, it can also be verified in Figure 5 that the BVID is only resolved up to a depth of 3.3 mm (see the colorbar), whereas one would expect that the delamination cone of impact damage extends through the whole thickness of the sample [10, 17], which is 5.5 mm in the current case.

3.2. Statistical time-energy gate (STEG)

To alleviate the shortcomings of the classical time gate approach in extracting the full extent of barely visible impact damage in composites, a non-constant-amplitude time gate based on the statistical nature of the A-scan signals of non-damaged scan points will be introduced in this section. The consecutive stages of this so-called Statistical Time-Energy Gating STEG algorithm are schematically presented in Figure 6. The four stages in the algorithm are explained in detail in the following four subsections.

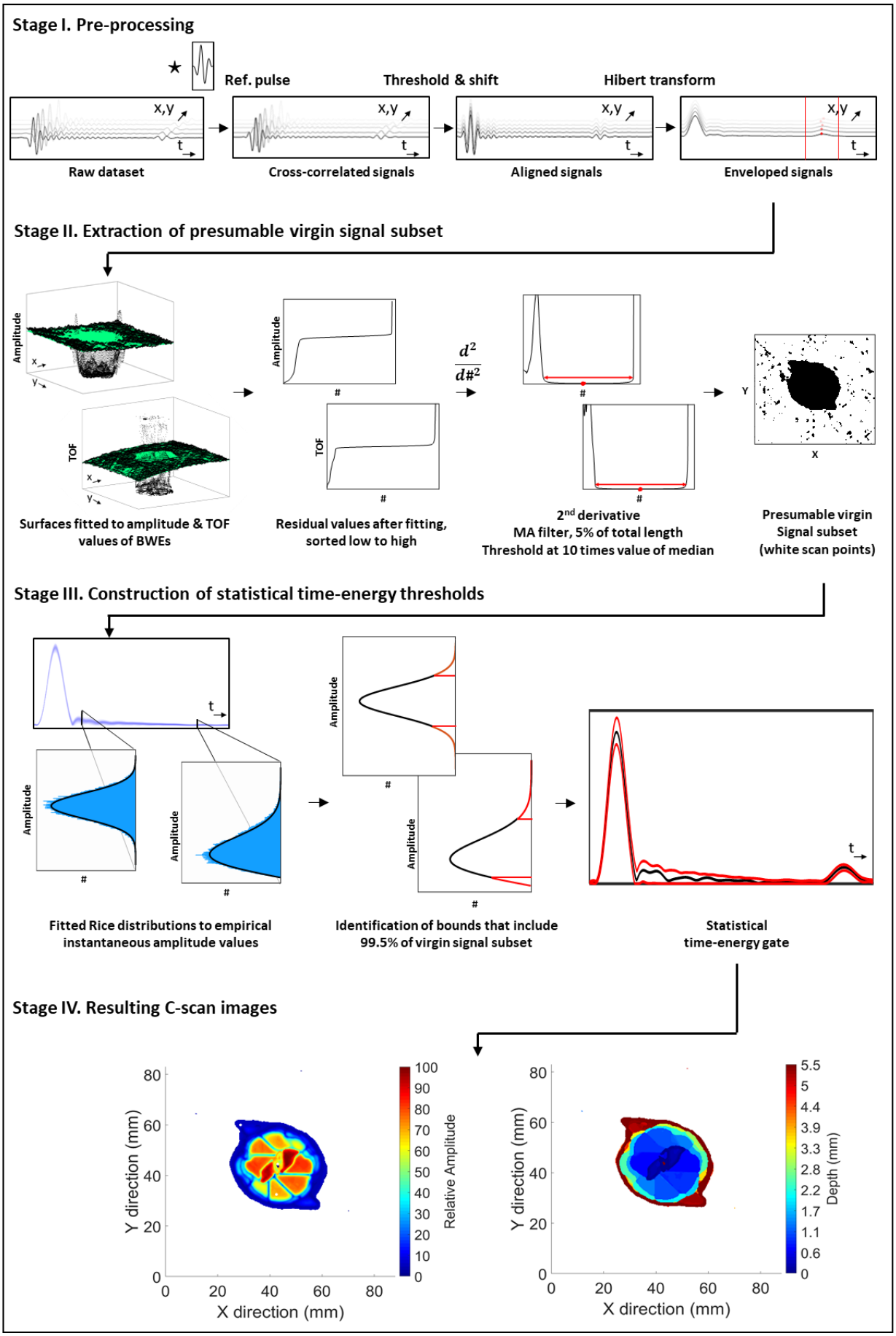

Figure 6: Schematic representation of the statistical time-energy gating algorithm

Stage I. Pre-processing

In the first stage, the acquired (raw) signals $s(t)$ are cross-correlated with the reference input signal $s_{ref}(t)$ (Figure 1a) in order to improve the signal quality and to suppress noise features. For better computational performance, the calculation is performed in the frequency domain.

$$\bar{s}(t) = \int s(\tau) s_{ref}(\tau - t) d\tau = \mathcal{F}^{-1}\left[S(f)\, S^*_{ref}(f)\right] \quad (1)$$

with $S(f)$ and $S_{ref}(f)$ the discrete Fourier transform of $s(t)$ and $s_{ref}(t)$ respectively. $\mathcal{F}^{-1}(\cdot)$ denotes the inverse discrete Fourier transform operator, and * symbolizes complex conjugation. Following the cross-correlation operation, a dynamic time gating approach is employed to compensate for possible curved geometry and/or non-horizontality of the sample [17, 53]. In other words, the signals $\bar{s}(t)$ are aligned in time dimension by putting a threshold on all signals at 60% of their maximum amplitude in order to align the signals at their FWE. The signals are then time-shifted accordingly (see Stage I in Figure 6).

Next, the analytic signal $\bar{s}_a(t)$ of the cross-correlated signal $\bar{s}(t)$ is calculated [54]:

$$\bar{s}_a(t) = \bar{s}(t) + i\bar{s}_h(t) \quad (2)$$

with $\bar{s}_h(t)$ the Hilbert transform, defined as

$$\bar{s}_h(t) = \frac{1}{\pi} \int_{-\infty}^{+\infty} \frac{\bar{s}(\tau)}{t - \tau} d\tau \quad (3)$$

For computational efficiency, the analytic signal is computed in the frequency domain [55]:

$$\bar{S}_a(f) = \begin{cases} 2\bar{S}(f), & f > 0 \\ 0, & f < 0 \\ \bar{S}(f), & f = 0 \end{cases} \quad (4)$$

with $\bar{S}(f)$ and $\bar{S}_a(f)$ the discrete Fourier transforms of $\bar{s}(t)$ and $\bar{s}_a(t)$, respectively.
The instantaneous amplitude A_{inst} is obtained as the magnitude of the analytic signal:

$$A_{inst}(t) = \sqrt{[Re(\bar{s}_a(t))]^2 + [Im(\bar{s}_a(t))]^2} \quad (5)$$

Note that the above steps are equal to the pre-processing steps used for standard TG imaging (e.g. Figure 5). In addition to these steps, the newly proposed STEG algorithm calculates for each scan point the instantaneous amplitude and the associated TOF of the BWE. These are found using a local

maximum comparison scheme, exploiting the higher amplitude of surface echoes as compared to interply echoes, and will be used in Stage II of the STEG algorithm (see next subsection).

Stage II. Extraction of presumable virgin signal subset

In Stage II of the STEG algorithm, a subset of presumably virgin signals is extracted from the instantaneous amplitude data using information from the BWEs of the signals (see last image in Stage I of Figure 6). To this end, a time gating window measuring twice the length of the reference input pulse is centered at the previously identified mean location of the BWEs. The maximum amplitude and corresponding TOF values within this time window are taken for all A-scan signals. For virgin signals, these values are expected to correspond to the local BWE signature, and should therefore be quite consistent over the sample. For defected signals, these values are expected to be irregularly distributed over a range of amplitude and TOF values. To account for variability in the local thickness, stiffness and/or density of the sample, a linear polynomial surface is fitted to the amplitude data and a quadratic surface to the TOF data using the least absolute deviations (LAD) method. The orders of the polynomials were empirically found to give reliable results, while the LAD method reduces sensitivity to outliers (damage scan points) [56].

The obtained fitting is presented in the first image in Stage II of Figure 6. Data points are shown in black, on which a green surface is fitted. It can be seen that the fitted surface closely matches the virgin area, and strongly deviates in the area of damage. After fitting, the residual values for both amplitude and TOF data are sorted in ascending order and subsequently differentiated twice. The two resulting curves are then rectified and smoothened using a moving average (MA) filter with a kernel size of 5% of the total number of scan points. The exact size of this kernel is of minor importance, similar results have been obtained by kernels with different sizes. Typically, the resulting curves show two peaks at the edges, which can be attributed to the poor polynomial fit in the damaged zone, and a wide 'low level' plateau in the middle corresponding to a good fit for the virgin material positions within the sample (see Stage II of Figure 6). Next, for both resulting curves, a threshold is adopted at ten times the median value, and the points on the plateaus below these thresholds are projected back to their spatial location. Again, the actual selected threshold value is of minor importance, similar results have been obtained for different threshold values. All A-scan signals that meet both conditions (amplitude and TOF) are then presumed to correspond to non-damaged area. This presumable virgin signal subset is colored white on the last image of Stage II in Figure 6. Finally, on the resulting 2D map of virgin signal locations, a median filter with a kernel size of 3 by 3 pixels is applied to reduce salt-and-pepper noise [57]. In the following Stage III, this identified subset of presumably virgin signals is used to define the confidence intervals for the instantaneous amplitude at every time instance, thus creating a time-varying set of statistical lower and upper bounds on the signals.

Stage III. Construction of statistical time-energy thresholds

Assuming that the acquired virgin signals are polluted with normally distributed noise features, their envelopes, or equivalently their instantaneous amplitudes A_{inst}, are well described by a Rice distribution with following probability density function PDF [41, 58]:

$$PDF\left(A_{inst}(t)|\nu(t)\,,\sigma(t)\right) \;=\; \frac{A_{inst}(t)}{\sigma^2(t)}\; e^{\frac{-\left(A_{inst}^2(t)\;+\nu^2(t)\;\right)}{2\sigma^2(t)}}\; I_0\left(\frac{A_{inst}(t)\;\nu(t)}{\sigma^2(t)}\right) \qquad (6)$$

with $\nu(t)$ the instantaneous amplitude of the noise-free signal at time t, $\sigma(t)$ the standard deviation of the noise at time t, and I_0 the modified Bessel function of the first kind with zero-order. Therefore, a Rice distribution is fitted at every time instance t on the instantaneous amplitude (for the presumably virgin signals) using maximum likelihood estimation (see the two examples in Stage III of Figure 6). This approach works well for the majority of time instances, but might encounter a problem in sections close to the BWE of the signals due to variability in the local thickness, stiffness and/or density of the composite.

To compensate for the sensitivity of the fit model to such small variations in this section of the time signal, the fitting is done separately for the time instances at and around the BWEs. First, the signals are realigned in time based on the TOF value associated with the BWE obtained from the surface fit in section 3.2b. The Rice distribution fitting procedure is then performed a second time on the empirical distributions obtained in this way, in a time range measuring twice the length of the reference pulse, centered around the mean BWE. Note that the variability in the material parameters influences not only the TOF of the backwall echoes, but also their amplitude (through attenuation). It was found that a Rice distribution still proved to be a good model for that time range.

As a result, for each time instance a Rice distribution is obtained which represents the stochastic nature of the instantaneous amplitude for presumably virgin A-scan signals. For the parts of the signals where two possible Rice distributions are available (from the FWE aligned dataset and from the BWE aligned dataset), the distributions obtained from alignment at the BWEs are used. This collection of Rice distributions allows to define time-varying reliability bounds to determine whether an A-scan signal corresponds to a healthy scan point or to a damaged scan point (see Figure 7). To construct the lower and upper bounds over the full time range, a confidence interval is defined at every time instance using the corresponding Rice distribution. The confidence intervals are defined by evaluating all distributions at uniformly calculated lower and upper limits (see Figure 7 part b), linked to the confidence level c as $(1-c)/2$ and $(1+c)/2$, respectively. With the probability of false alarm (PFA) defined as the probability of falsely classifying a virgin signal as defected, the confidence level is chosen such that the PFA for the virgin signal subset equals 0.5 % (which was empirically found to be a good value for this parameter). This means that c is chosen such that 99.5 % of the signals in the presumable virgin subset are contained inside the resulting time-energy gate. To this end, an iterative process is introduced. To start off the iteration, an initial guess of the confidence level is taken as $\sqrt[L]{1-PFA}$, with L the length of the signals (in number of samples), and the corresponding intermediate time-energy gate is constructed. This gate is then used to evaluate the presumable virgin subset, after which the confidence level is iterated, using the regula falsi method [59], until the specified PFA is reached or until the confidence level exceeds $1-e^{-14}$ (stop condition) (see Figure 7 part c). This iterative process finally leads to the suitable lower and upper bounds for the time-energy gate (see Figure 7 part d). If a signal is fully confined in this time-energy band, it is classified as a virgin signal. Contrarily, if a signal (partially) falls outside the bounds of the time-energy gate, it is conclusively classified as a signal associated to a local defect feature.

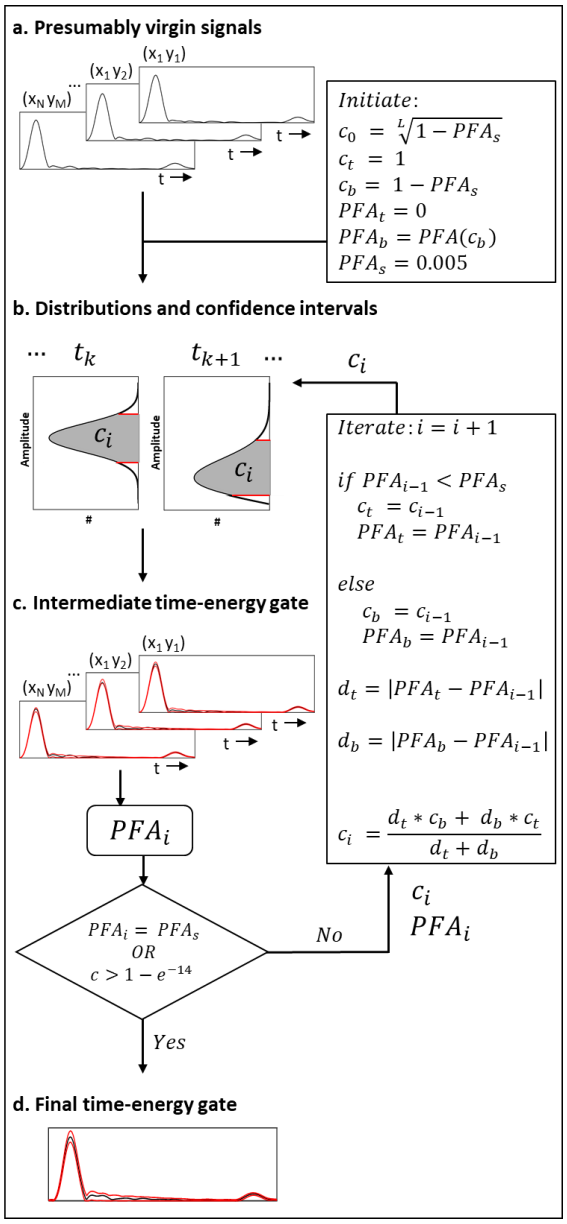

Figure 7: Schematic representation of the iterative construction of the statistical time-energy gate

Stage IV. Resulting C-scan images

For the resulting set of identified defected signals, C-scan imaging is performed by selecting their highest amplitude outside the time-energy band, along with the associated TOF value. As previously, the TOF values are converted to depth values. On the resulting amplitude and depth C-scan images, a median filter with kernel size 3 by 3 pixels is applied to smoothen the image and to remove isolated scan points. The resulting C-scan images of the proposed STEG procedure for the CFRP-1 sample are shown in Figure 8. In contrast to the classical TG imaging (see Figure 5), the damage map resulting from the STEG algorithm agrees well with the extracted damage contour from the double-through transmission imaging. Apart from the (global) lateral sizing of the impact damage, the STEG imaging method also successfully images the delamination cone through the full thickness of the composite laminate (note the range of the color bar in Figure 8b). Moreover, the STEG method automatically filters out the signal variability of virgin signals by classifying them as non-defected, as can be seen by

the uniform white background in Figure 8b. This is in strong contrast to the classical TG method (see Figure 5) which generates C-scan images with background noise due to the heterogenous and multi-layered nature of the composite laminate. A minor downside of the STEG procedure concerns the disclosure of wrongly classified damaged pixels, as indicated by the arrow in Figure 8b. Of course, a small amount of wrongly classified scan points could have been expected considering the use of a PFA of 0.5% for constructing the bounds of the statistical time-energy gate.

In terms of computational efficiency, the STEG procedure takes around 100 s for the given dataset on a computer with Intel Xeon Gold 6146 CPU @ 3.2 GHz. Note that the computational efficiency may improve significantly by considering CPU parallelization and/or GPU calculation. Also down-sampling in time domain of the ultrasonic dataset could relax the high computational intensity of the Rice fitting procedure, after which appropriate up-sampling schemes can be used to project the fitted statistical distributions back on the original data.

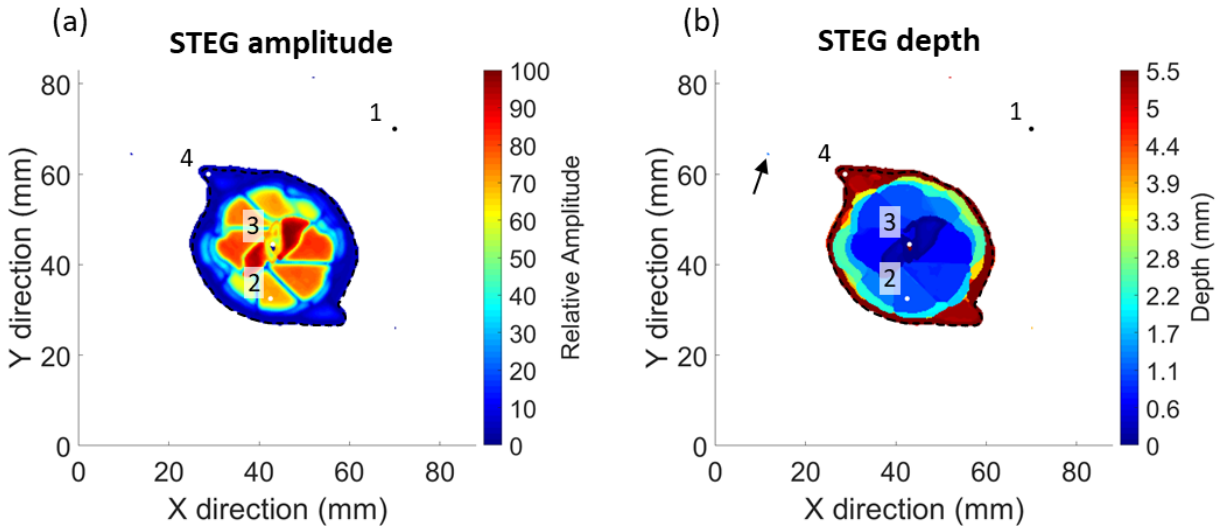

Figure 8: (a) Amplitude and (b) depth C-scan using the proposed STEG method. The damage contour, extracted from the double-through transmission amplitude C-scan, is superposed as a black dashed line.

4. Results and discussion

4.1. Validation on different composite samples

Apart from the CFRP-1 sample, the STEG algorithm is also applied on two other impacted samples, CFRP-2 and CFRP-3 (see Table 1). In order to underline the robustness of the STEG method, the previously defined parameters (e.g., MA filter and kernel size for median filter, see section 3.2) were not changed for these different samples. The resulting C-scan images for the different damage assessment procedures can be seen in Figure 9.

For the CFRP-2 sample (cross-ply lay-up impacted with an energy of 6.0 J), a comparison of the double-through transmission amplitude C-scan (Figure 9b) and the amplitude and depth C-scan images from classical TG pulse-echo imaging (Figure 9c-d) clearly exposes the inadequacy of the latter. Both shallow and deep defects are not detected in a satisfactory manner. The inset in Figure 9d shows that the deeper delaminations are not resolved in a proper manner. The amplitude and depth C-scans obtained by way of the STEG imaging (Figure 9e-f) on the other hand shows the full extent of the barely visible

impact damage. The inset in Figure 9f reveals that the STEG algorithm detects small neighboring delamination fragments through the whole depth of the laminate.

For the CFRP-3 sample (quasi-isotropic lay-up impacted with an energy of 15.5 J), the high impact energy led to a considerably larger size of the induced damage. It should be noted that this presents a challenge for the STEG algorithm. Indeed, when sorting the residual amplitude and TOF values of the BWEs in the STEG procedure (see Stage II in Figure 6 and subsection 3.2), it is assumed that the majority of the signals stem from virgin material. As this was not the case for this CFRP-3 sample, it was necessary to manually select an area of mainly healthy wave signals, e.g., the top part of the inspection area, and to feed these signals to the STEG algorithm. Apart from this manual selection, the exact same settings in the STEG algorithm were employed as in previous cases. The obtained results are reported in the bottom row of Figure 9. Again, these results confirm the superiority of the STEG approach for imaging the full extent of the impact damage, both in lateral and in depth dimension. This can be especially appreciated by the shown inset for the depth C-scan images. From the imaging results using the TG approach (see inset in Figure 9j), it can be seen that the deep delaminations are not fully resolved. Further, the TG method indicates that neighboring delaminations are somehow disconnected from each other. This is physically not what one would expect to happen. The imaging results from the STEG method (see the inset in Figure 9l) present an improved view on the damage zone, in which delamination fragments at different depths connect to each other.

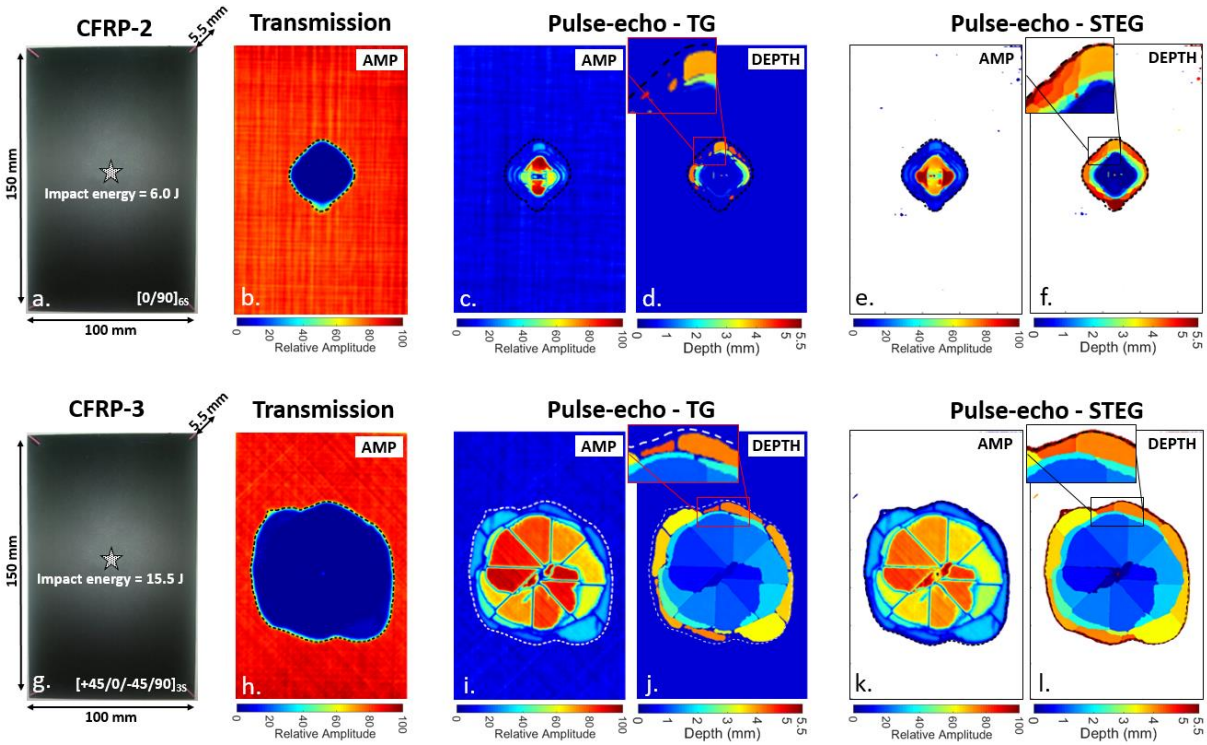

Figure 9: C-scan images using different damage assessment procedures for sample CFRP-2 (top row) and CFRP-3 (bottom row): (a,g) Picture of samples; (b,h) Double through-transmission amplitude; Pulse-echo TG method (c,i) amplitude and (d,j) depth; Pulse-echo STEG method (e,k) amplitude and (f,l) depth. The damage contour, extracted from the double-through transmission amplitude C-scan, is superposed as a dashed line.

4.2. Quantitative performance analysis

To objectively compare the performance of the different techniques, binary damage maps are constructed from which indicative metrics can be derived. For the double-through transmission result, pixels are identified as defected if they exhibit a 3 dB amplitude drop compared to the mean amplitude of non-defected area. This damage map is considered as the ground truth, and is used to benchmark against the other techniques. For the time gated pulse-echo data, pixels are identified as damaged if the amplitude is 3 dB higher than the mean amplitude of the non-damaged area, or if the corresponding TOF value is higher than the TOF of the non-damaged area. Hence, the final damage map is the union of both. For the STEG pulse-echo data, the damaged pixels naturally arise from the algorithm, and they are straightforwardly assigned to a binary representation. The three binary damage maps for sample CFRP-1 are shown in Figure 10, with black and white color representing healthy and defected pixels respectively. It can be visually confirmed that these three binary representations have different shapes.

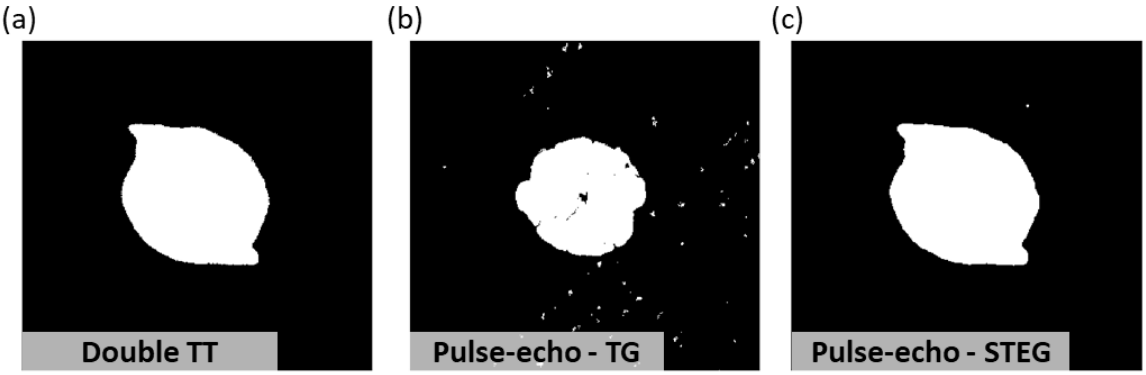

Figure 10: Binary damage maps for CFRP-1: (a) double through-transmission, (b) TG pulse-echo, (c) STEG pulse-echo

Subsequently, four different objective metrics are defined to assess the defect detectability of the different approaches:

- The Probability of Detection (POD) gives the probability that a defect pixel (in the benchmark, double TT damage map) is also classified as such by the TG or STEG pulse-echo imaging method. It is defined as:

$$POD = \frac{TP}{TP + FN} \cdot 100\ [\%] \tag{7}$$

with TP the number of true positive pixels and FN the number of false negative pixels.

- The Probability of False Alarm (PFA) gives the probability that a sound pixel (in the benchmark, double TT damage map) is wrongly classified as being defected by the TG or STEG pulse-echo imaging method. It is defined as:

$$PFA = \frac{FP}{FP + TN} \cdot 100\ [\%] \tag{8}$$

with FP the number of false positive pixels and TN the number of true negative pixels.

- The Jaccard Index (JI) is a metric which determines the similarity (or dissimilarity) between two samples. Note that this criterion is sometimes also referred to as the Tanimoto index. The JI is defined as:

$$JI = \frac{TP}{TP + FP + FN} \cdot 100\ [\%] \tag{9}$$

- The Depth Range (DR) represents the relative depth range over which defects are detected. It is defined as the following ratio:

$$DR = \frac{D_{max} - D_{min}}{D_{tot}} \cdot 100\ [\%] \tag{10}$$

with D_{max} and D_{min} the maximum and minimum depth of defects found by the imaging method, and D_{tot} the total sample thickness.

Ideally, the POD metric is as close to 100% as possible, while maintaining the PFA metric as close to 0% as possible. The JI metric should ideally also be close to 100%. Considering that an impact on CFRP induces a delamination cone which typically extends over the full depth range of the material [17], it is assumed that the DR metric should ideally be as close to 100% as possible. Note that even though the binary defected areas in Figure 10a and Figure 10c are very similar, a subtle difference exists at the defect edge, mainly attributed to the choice of the 3 dB threshold approach. A significant amount of the false positive and false negative pixels of the STEG method is located at these edges and therefore influences the exact value of the POD, PFA and JI metrics. The analyzed values of the four metrics for both the TG and STEG method are shown in Table 2 for the various CFRP samples. The row *Perfect result* shows the ideal value of the metrics (double through-transmission data taken as benchmark). The STEG method clearly shows increased defect detectability, i.e., higher POD, with respect to TG. STEG consistently detects defects over the full depth range, while only few false positive pixels are present resulting in a small PFA. In terms of the JI metric, the STEG method provides large values indicating that the obtained damage map shows high similarity to the damage map obtained by the double-through transmission method. This is in clear contrast to the results obtained by the TG method, showing rather intermediate Jaccard index values. These observations hold for the various inspected CFRP samples. Of course, the exact values of the reported four metrics will slightly change based on the adopted definition to binarize the damage maps. However, it has been verified that similar conclusions can be drawn if the damage binarization is done based on other thresholds (e.g. 6 dB amplitude drop).

Table 2: Comparison of image metrics for TG and STEG pulse-echo assessments.

		Perfect result	CFRP-1 (QI – 5.4 J)	CFRP-2 (CP – 6.0 J)	CFRP-3 (QI – 15.5 J)
POD [%]	TG	100	67.9	55.8	90.1
	STEG	100	99.7	97.5	99.9
PFA [%]	TG	0	0.4	0.0	0.0
	STEG	0	0.2	0.3	1.0
JI [%]	TG	100	64.1	55.8	90.1
	STEG	100	98.4	93.7	98.4
DR [%]	TG	100	53.0	77.1	72.6
	STEG	100	100	100	100

4.3. Robustness

From the above case studies, it is clear that the proposed STEG method is superior in both sizing and depth determination of impact damage in CFRP laminates. In this section, an analysis on the robustness of the STEG algorithm is performed. The analysis is carried out on the datasets corresponding to an impact height of 0.1 m, i.e., samples CFRP-1 and CFRP-2 are used.

a. Defect-to-sound ratio (DSR)

In the first part of the robustness analysis, the scanned area was narrowed down such that the ratio between defect area and sound area increases. For different defect-to-sound ratios (DSR), the resultant POD and PFA metrics for the TG and the STEG images are displayed in Figure 11.

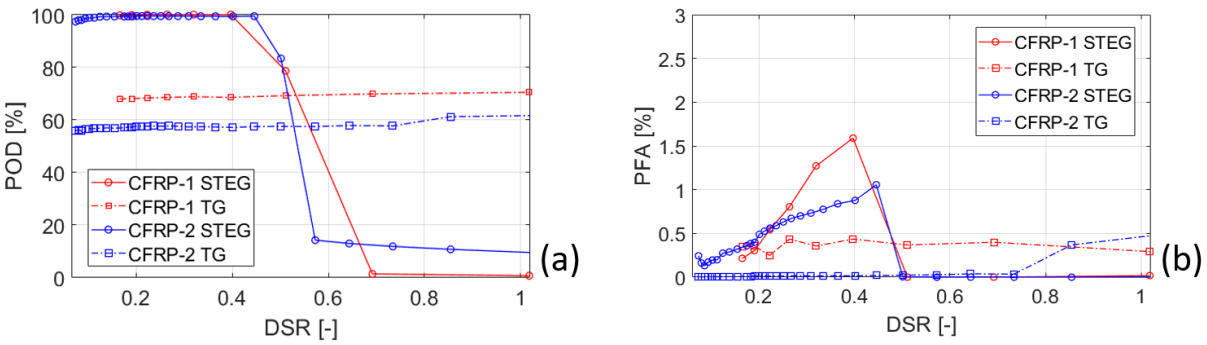

Figure 11: Influence of defect-to-sound ratio DSR on the performance of the TG and STEG methods: (a) Probability of Detection POD and (b) Probability of False Alarm PFA.

It can be seen that the classical TG results remain stable over the whole DSR, but only at an intermediate POD of about 65%. The PFA values remain below 0.5% over the whole DSR range.

For the STEG method on the other hand, the POD is close to 100% for DSR values up to 0.4. For this range of DSR, the PFA slightly increases due to a high occurrence of false positive pixels at the defect edges (as explained in section 4.2), which represent a higher fraction of all pixels as the DSR increases. When the DSR increases above 0.5, both the POD and PFA suddenly drop to low values. This is related to a breakdown in the STEG method, more particularly in the automated procedure to identify the presumably virgin scan points. The same difficulty was reported during the analysis of sample CFRP-3, for which the defect-to-sound ratio was 0.59. As mentioned in section 4.1, this breakdown of the STEG

method can be easily solved by manual selection of a virgin area. Though inconvenient, it is not considered a problem for the proposed STEG method, as in real-world applications the DSR of inspected parts is usually much smaller than 0.5. Furthermore, in a serialized inspection setup, a database of known virgin signals could be set up using sound samples, making the extraction of virgin data from the sample under inspection unnecessary.

b. Signal-to-noise ratio

In the second part of the robustness analysis, the noise resistance of the proposed STEG method is investigated. A representative A-scan signal from sample CFRP-1 (point 1 on Figure 3) is shown in Figure 12a. Here, the SNR is defined as the ratio of the signal power P_s to the noise power P_n and is expressed in decibels (dB):

$$SNR = 10 \cdot \log_{10}\left(\frac{P_s}{P_n}\right) \tag{10}$$

The power of a discrete-time (digitized) signal $s(t)$ is defined as:

$$P_s = \frac{\sum_{t=0}^{t_{max}} s^2(t)}{L} \tag{11}$$

with L the total signal length (in number of samples). The signal power is calculated from the recorded pulse-echo signal using the time interval (t = 0 → 4.35 µs) shown in Figure 12a, while the noise power was calculated in a time interval where no response signal was observed. This results in a typical SNR value of ~32 dB for the recorded A-scan signals. To understand the noise resistance of the proposed STEG procedure, the experimental datasets have been polluted with additional white Gaussian noise, i.e., noise with a uniform spectral density and a Gaussian amplitude distribution. Figure 12a, shows the resulting A-scan signals for different levels of noise addition. The amplitude C-scan image obtained by the TG method and the proposed STEG method are presented in Figure 12b and Figure 12c respectively. While the TG method yields results which remain more or less stable, the results obtained from the STEG method change. It seems that for lower SNR values, the STEG procedure cannot capture all details of the impact damage anymore, especially the deep delamination fragments are underrepresented. Comparison of the TG and STEG results at the very low SNR values (bottom two rows of Figure 12) seems to indicate that the STEG imaging method lost its outperformance, and provides a damage imaging which is comparable to the results of the classical TG method.

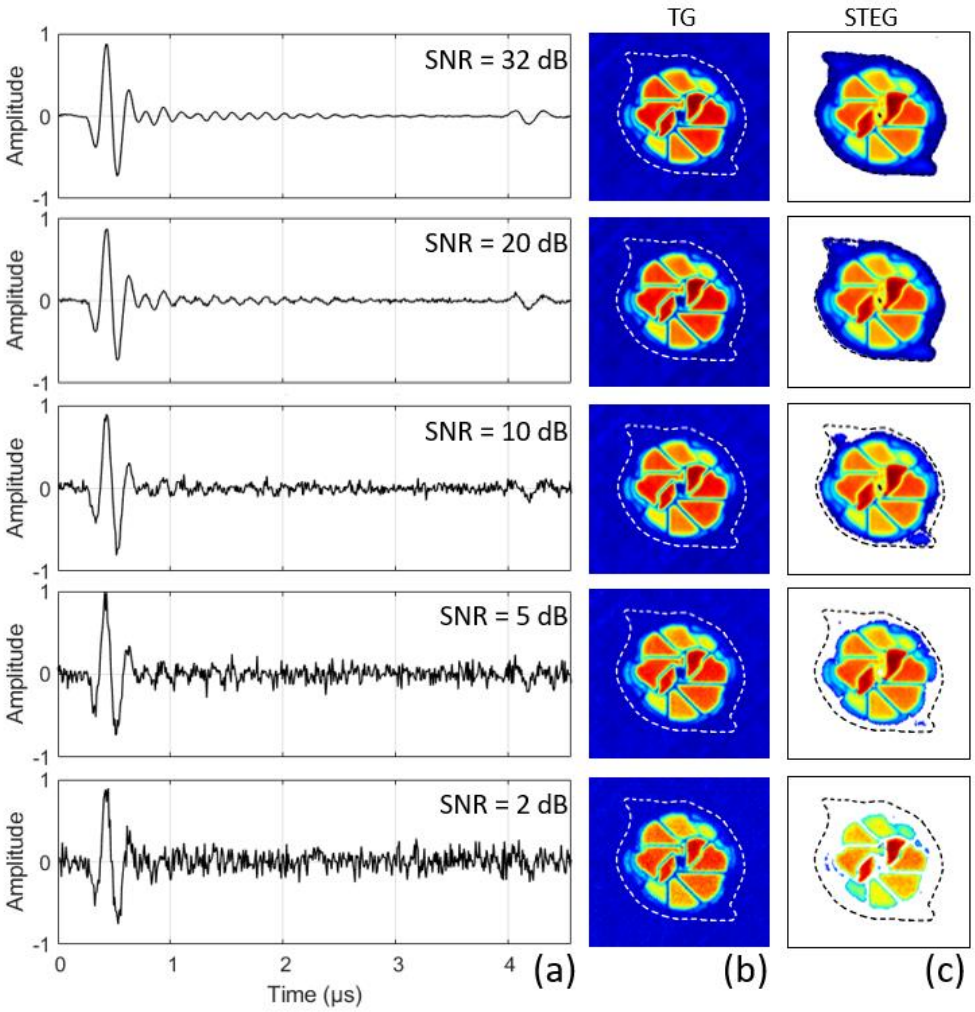

Figure 12: Results for different SNR levels: (a) representative A-scan signals, and pulse-echo amplitude C-scan representation using (b) classical Time Gate TG and (c) proposed Statistical Time-Energy Gate STEG. From top to bottom the SNR equals: 32 db (original recording), 20 dB, 10 dB, 5 dB and 2 dB.

To get more conclusive results on the noise resistance of the STEG method, both the TG and STEG approach for damage imaging have been applied on the dataset of CFRP-1 and CFRP-2. These datasets were polluted with various levels of white Gaussian noise, resulting in a SNR which ranges from 32 dB (original experiment) to 1 dB. To account for the stochastic nature of the added noise, the damage imaging procedure has been repeated 10 times. The mean value and standard deviation for the POD and PFA are reported in Figure 13.

For the classical TG method, the POD and PFA remain stable for both samples for SNR values as low as about 7 dB. Note however that the POD has only intermediate values of around 60%. When the noise level increases further, the POD increases which might seems counterintuitive. Though, evaluation of the PFA metric, which also increases, puts this in perspective. In other words, for such high noise levels the TG method basically detects a significant portion of healthy pixels as being defected.

For the STEG method on the other hand, the POD starts at values close to 100% indicating its high performance in accurate damage sizing. For increased noise levels, the POD slowly decreases. This is understood by the broadening of the bounds of the statistical time-energy gate in order to encompass 99.5% of the virgin signals. The weakest defect echoes (corresponding to the deepest defects) then

easily go undetected. Once the SNR of the ultrasonic dataset decreases below 5 dB, the POD for the STEG method drops to values below 65%. At such low SNR values, the STEG imaging basically lost its outperformance, and converged to the results obtained by the classical TG method (see also Figure 12, 4th and 5th row). Further reduction of the SNR makes the STEG method very unreliable. For such low SNR values, the BWE simply gets buried in the noise and the automated virgin signal extraction becomes impossible and as such the STEG algorithm breaks down. The PFA metric remains stable at a value of ~0.3% up till a SNR of 3 dB. For lower SNR, the PFA drops to 0% because of the breakdown of the STEG algorithm.

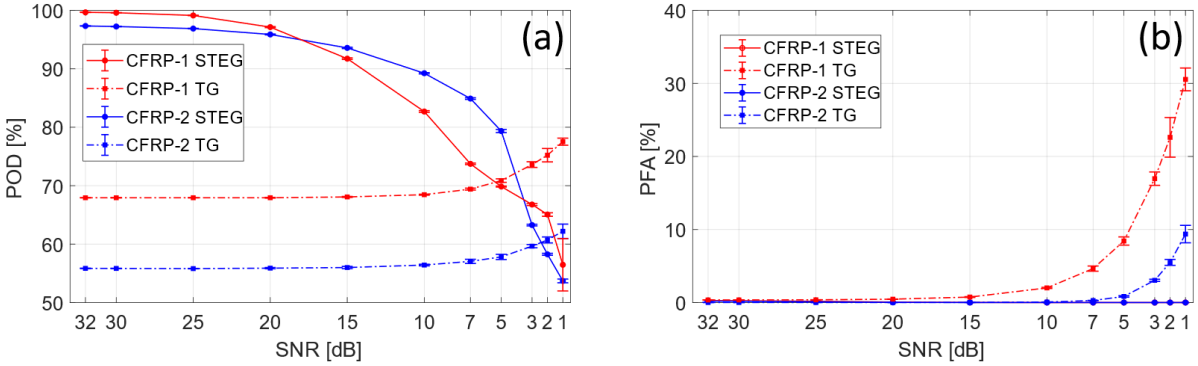

Figure 13: Performance of the classical TG and proposed STEG methods in function of signal-to-noise ratio: (a) Probability of Detection POD and (b) Probability of False Alarm PFA.

5. Conclusion

A novel automated Statistical Time-Energy Gating (STEG) method for evaluating pulse-echo ultrasound is proposed. In contrast to the classical Time Gating (TG) method, the proposed STEG method makes use of a probabilistic data analysis. First a presumable set of virgin signals is identified using a clustering method. In the unlikely case that the inspection area predominantly exists of damage, the clustering method shows poor performance and instead a manual selection of a representative virgin area is required. Through maximum likelihood estimation, optimal Rice distributions are obtained which represent the stochastic nature of the instantaneous amplitude of virgin signals. Then, by a preset probability of false alarm, reliability intervals over the full time range of interest are obtained which prescribe the upper and lower bound of the statistical time-energy gate. The resulting statistical time-energy band can cope with noise features as well as with the heterogeneous and layered structure of composite laminates. This allows to robustly distinguish healthy signals from defected signals, resulting in superior quality amplitude and TOF (or depth) C-scan images.

The STEG method was demonstrated on several 24-layer CFRP samples (quasi-isotropic and cross-ply stacking) containing various levels of barely visible impact damage. Double through-transmission amplitude C-scan images were taken as the ground truth for defect sizing, and served as benchmark against the classical TG and STEG pulse-echo methods. The obtained results show that the novel STEG procedure outperforms the classical TG method in terms of both sizing and depth determination of complex barely visible impact damage in CFRPs. Especially for imaging very shallow defects, very deep defects and neighboring delaminations, the proposed STEG method shows excellent performance. Objective detection metrics (Probability of Detection POD, Probability of False Alarm PFA, Jaccard Index JI and Depth Range DR) have been evaluated, confirming the high performance of the STEG

method for the different studied test cases. Finally, the good noise-resistance of the STEG method for accurate damage imaging was demonstrated.

It is anticipated that the novel STEG method could help in developing and validating advanced numerical impact damage models, and in obtaining a more reliable estimate of the remaining useful lifetime of impacted CFRP laminates.

Acknowledgements

The authors gratefully acknowledge the financial support from the Fund for Scientific Research-Flanders (FWO Vlaanderen, grant G066618N) and the Ghent University Special Research Fund (BOF, grant 01N01719). The authors further acknowledge the ICON project ALMA (HBC.2018.0427) which fits in the research program STREAM funded by SIM (Strategic Initiative Materials in Flanders) and VLAIO (Flemish government agency Innovation & Entrepreneurship).

Data availability

The raw/processed data required to reproduce these findings cannot be shared at this time as the data also forms part of an ongoing study.

References

1. Pérez, M.A., et al., *High-velocity ice impact damage quantification in composite laminates using a frequency domain-based correlation approach.* Mechanical Systems and Signal Processing, 2021. **147**.
2. Solodov, I., M. Rahammer, and M. Kreutzbruck, *Analytical evaluation of resonance frequencies for planar defects: Effect of a defect shape.* NDT & E International, 2019. **102**: p. 274-280.
3. Poelman, G., et al., *Adaptive spectral band integration in flash thermography: Enhanced defect detectability and quantification in composites.* Composites Part B: Engineering, 2020. **202**.
4. Fleuret, J.R., et al., *Independent Component Analysis Applied on Pulsed Thermographic Data for Carbon Fiber Reinforced Plastic Inspection: A Comparative Study.* Applied Sciences, 2021. **11**(10): p. 4377.
5. de Oliveira, B.C.F., et al., *Improved impact damage characterisation in CFRP samples using the fusion of optical lock-in thermography and optical square-pulse shearography images.* NDT & E International, 2020. **111**.
6. Anisimov, A.G. and R.M. Groves, *Extreme shearography: Development of a high-speed shearography instrument for quantitative surface strain measurements during an impact event.* Optics and Lasers in Engineering, 2021. **140**: p. 106502.
7. Sha, G., et al., *Guided wavefield curvature imaging of invisible damage in composite structures.* Mechanical Systems and Signal Processing, 2021. **150**: p. 107240.
8. Segers, J., et al., *Nonlinear local wave-direction estimation for in-sight and out-of-sight damage localization in composite plates.* NDT & E International, 2021. **119**: p. 102412.
9. Lugovtsova, Y., et al., *Damage Quantification in an Aluminium-CFRP Composite Structure using Guided Wave Wavenumber Mapping: Comparison of Instantaneous and Local Wavenumber Analyses.* NDT & E International, 2021: p. 102472.
10. Morokov, E., et al., *High resolution ply-by-ply ultrasound imaging of impact damage in thick CFRP laminates by high-frequency acoustic microscopy.* Composite Structures, 2021. **256**.
11. Spytek, J., et al., *Multi-resolution non-contact damage detection in complex-shaped composite laminates using ultrasound.* NDT & E International, 2020. **116**: p. 102366.
12. Yang, X., et al., *Comparative study of ultrasonic techniques for reconstructing the multilayer structure of composites.* NDT & E International, 2021: p. 102460.

13. Smith, R.A., et al., *Automated analysis and advanced defect characterisation from ultrasonic scans of composites.* Insight - Non-Destructive Testing and Condition Monitoring, 2009. **51**(2): p. 82-87.
14. Eren, E., S. Kurama, and I. Solodov, *Characterization of porosity and defect imaging in ceramic tile using ultrasonic inspections.* Ceramics International, 2012. **38**(3): p. 2145-2151.
15. D'Orazio, T., et al., *Automatic ultrasonic inspection for internal defect detection in composite materials.* Ndt & E International, 2008. **41**(2): p. 145-154.
16. Wronkowicz, A., K. Dragan, and K. Lis, *Assessment of uncertainty in damage evaluation by ultrasonic testing of composite structures.* Composite Structures, 2018. **203**: p. 71-84.
17. Spronk, S.W.F., et al., *Comparing damage from low-velocity impact and quasi-static indentation in automotive carbon/epoxy and glass/polyamide-6 laminates.* Polymer Testing, 2018. **65**: p. 231-241.
18. Thorsson, S.I., A.M. Waas, and M. Rassaian, *Low-velocity impact predictions of composite laminates using a continuum shell based modeling approach Part b: BVID impact and compression after impact.* International Journal of Solids and Structures, 2018. **155**: p. 201-212.
19. Daelemans, L., et al., *Electrospun nanofibrous interleaves for improved low velocity impact resistance of glass fibre reinforced composite laminates.* Materials & Design, 2018. **141**: p. 170-184.
20. Post, W., et al., *Non-destructive monitoring of delamination healing of a CFRP composite with a thermoplastic ionomer interlayer.* Composites Part A: Applied Science and Manufacturing, 2017. **101**: p. 243-253.
21. Caputo, F., et al., *Numerical study for the structural analysis of composite laminates subjected to low velocity impact.* Composites Part B: Engineering, 2014. **67**: p. 296-302.
22. Sun, X.C. and S.R. Hallett, *Failure mechanisms and damage evolution of laminated composites under compression after impact (CAI): Experimental and numerical study.* Composites Part A: Applied Science and Manufacturing, 2018. **104**: p. 41-59.
23. Daryabor, P. and M.S. Safizadeh, *Image fusion of ultrasonic and thermographic inspection of carbon/epoxy patches bonded to an aluminum plate.* NDT & E International, 2017. **90**: p. 1-10.
24. Jin, S.J., et al., *Quantitative detection of shallow subsurface cracks in pipeline with time-of-flight diffraction technique.* NDT & E International, 2021. **118**.
25. Carcreff, E., et al., *A linear model approach for ultrasonic inverse problems with attenuation and dispersion.* IEEE transactions on ultrasonics, ferroelectrics, and frequency control, 2014. **61**(7): p. 1191-203.
26. Hauffe, A., F. Hähnel, and K. Wolf, *Comparison of algorithms to quantify the damaged area in CFRP ultrasonic scans.* Composite Structures, 2020. **235**: p. 111791.
27. Sadeghi, M.Z., et al., *Damage detection by double-sided ultrasonic assessment in low-velocity impacted CFRP plates.* Composite Structures, 2019. **208**: p. 646-655.
28. Dalitz, C., R. Pohle-Frohlich, and T. Michalk, *Point spread functions and deconvolution of ultrasonic images.* IEEE transactions on ultrasonics, ferroelectrics, and frequency control, 2015. **62**(3): p. 531-44.
29. Rangarajan, R., C.V. Krishnamurthy, and K. Balasubramaniam, *Ultrasonic imaging using a computed point spread function.* IEEE transactions on ultrasonics, ferroelectrics, and frequency control, 2008. **55**(2): p. 451-64.
30. Florea, M.I., et al., *An Axially Variant Kernel Imaging Model Applied to Ultrasound Image Reconstruction.* IEEE Signal Processing Letters, 2018. **25**(7): p. 961-965.
31. R. Drai, F.S., M. Khelil, A. Benchaala, *Elaboration of some signal processing algorithms in ultrasonic techniques: application to materials NDT.* Ultrasonics, 2000. **38**.
32. M. Parrilla, J.J.A., and C. Fritsch, *Digital Signal Processing Techniques for High Accuracy Ultrasonic Range Measurements.* IEEE Transactions on Instrumentation and Measurement, Aug. 1991. **40**(4): p. 759-763.

33. Shakibi, B., et al., *Resolution enhancement of ultrasonic defect signals for crack sizing.* NDT & E International, 2012. **52**: p. 37-50.
34. Honarvar, F., et al., *Improving the time-resolution and signal-to-noise ratio of ultrasonic NDE signals.* Ultrasonics, 2004. **41**(9): p. 755-763.
35. Kleinert, W., *Defect Sizing Using Non-destructive Ultrasonic Testing Applying Bandwidth-Dependent DAC and DGS Curves*. 2016: Springer.
36. Pelivanov, I., et al., *High resolution imaging of impacted CFRP composites with a fiber-optic laser-ultrasound scanner.* Photoacoustics, 2016. **4**(2): p. 55-64.
37. Segreto, T., R. Teti, and V. Lopresto, *Non-Destructive Testing of Low-Velocity Impacted Composite Material Laminates through Ultrasonic Inspection Methods*, in *Characterizations of Some Composite Materials*. 2019.
38. Aymerich, F. and S. Meili, *Ultrasonic evaluation of matrix damage in impacted composite laminates.* Composites Part B: Engineering, 2000. **31**(1): p. 1-6.
39. Qin, L., et al., *3D ultrasonic imaging based on synthetic aperture focusing technique and space-dependent threshold for detecting submillimetre flaws in strongly scattering metallic materials.* NDT & E International, 2021. **124**: p. 102523.
40. Song, Y., et al., *Statistics associated with the scattering of ultrasound from microstructure.* Ultrasonics, 2017. **80**: p. 58-61.
41. Song, Y., et al., *Flaw detection with ultrasonic backscatter signal envelopes.* The Journal of the Acoustical Society of America, 2019. **145**(2): p. EL142-EL148.
42. Rodrigues, L.F.M., et al., *Carburization level identification in industrial HP pipes using ultrasonic evaluation and machine learning.* Ultrasonics, 2019. **94**: p. 145-151.
43. Meng, M., et al., *Ultrasonic signal classification and imaging system for composite materials via deep convolutional neural networks.* Neurocomputing, 2017. **257**: p. 128-135.
44. Yang, X., B.-F. Ju, and M. Kersemans, *Assessment of the 3D ply-by-ply fiber structure in impacted CFRP by means of planar Ultrasound Computed Tomography (pU-CT).* Composite Structures, 2022. **279**: p. 114745.
45. *Measuring the Damage Resistance of a Fiber-reinforced Polymer Matrix Composite to a Drop-weight Impact Event*. 2005, ASTM International: West Conshohocken, PA.
46. Summerscales, J., *Non-destructive testing of fibre-reinforced plastics composites*. Vol. 2. 1990: Springer Science & Business Media.
47. Felice, M.V. and Z. Fan, *Sizing of flaws using ultrasonic bulk wave testing: A review.* Ultrasonics, 2018. **88**: p. 26-42.
48. *Standard Practice for Ultrasonic Testing of Flat Panel Composites and Sandwich Core Materials Used in Aerospace Applications*. 2012, ASTM International: West Conshohocken, PA.
49. Murphy, R., *Ultrasonic defect-sizing using decibel drop methods. II*. 1987, Atomic Energy Control Board.
50. Ciorau, P. and O.P. Generation, *Comparison between -6 dB and -12 dB amplitude drop techniques for length sizing.* e-Journal of Nondestructive Testing (NDT), 2011. **11**.
51. Kumaran, S. and B. Rani, *Application of 6db Drop Technique to Estimate the Width of Sub Assembly Ring Top Using Pulse Echo Ultrasonic Technique.* International Journal of Engineering and Technology, 2013. **5**(6): p. 4771-4775.
52. Ma, M., et al., *High Precision Detection Method for Delamination Defects in Carbon Fiber Composite Laminates Based on Ultrasonic Technique and Signal Correlation Algorithm.* Materials, 2020. **13**(17): p. 3840.
53. Smagulova, D., L. Mazeika, and E. Jasiuniene, *Novel Processing Algorithm to Improve Detectability of Disbonds in Adhesive Dissimilar Material Joints.* Sensors, 2021. **21**(9): p. 3048.
54. Hlawatsch, F. and F. Auger, *Time-frequency analysis*. 2008: Wiley Online Library.
55. Marple, L., *Computing the Discrete-Time "Analytic" Signal via FFT.* IEEE Transactions on signal processing, 1999. **47**(9): p. 2600-2603.
56. Dodge, Y., *The Concise Encyclopedia of Statistics*. 2008: Spinger.

57. Gonzalez, R. and R. Woods, *Digital Image Processing*. 3rd. ed. 2009: Pearson Education International.
58. Rice, S.O., *Mathematical Analysis of Random Noise.* Bell System Technical Journal, 1945. **24**(1): p. 46-156.
59. Press, W.H., et al., *Numerical recipes 3rd edition: The art of scientific computing*. 2007: Cambridge university press.